optica

All-electronic terahertz nanoscopy

CLEMENS LIEWALD,[1,2] STEFAN MASTEL,[3] JEFFREY HESLER,[4] ANDREAS J. HUBER,[5] RAINER HILLENBRAND,[6,7] AND FRITZ KEILMANN[1,*]

[1]Fakultät für Physik & Center for NanoScience (CeNS), Ludwig-Maximilians-Universität, 80539 München, Germany
[2]Nanosystems Initiative Munich, 80799 München, Germany
[3]CIC nanoGUNE, 20018 Donostia-San Sebastián, Spain
[4]Virginia Diodes Inc., Charlottesville, Virginia 22901, USA
[5]Neaspec GmbH, 82512 Martinsried, Germany
[6]CIC nanoGUNE and UPV/EHU, 20018 Donostia-San Sebastián, Spain
[7]IKERBARSQUE, Basque Foundation of Science, 48013 Bilbao, Spain
*Corresponding author: fritz.keilmann@lmu.de

Probing conductivity in a contactless way with nanoscale resolution is a pressing demand in such active fields as quantum materials, superconductivity, and molecular electronics. Here, we demonstrate a laser- and cryogen-free microwave-technology-based scattering-type scanning near-field optical microscope powered by an easily aligned free-space beam with a tunable frequency up to 0.75 THz. It uses Schottky diode components to record background-free amplitude and phase nano-images, for the first time in the terahertz range, which is uniquely sensitive for assessing conduction phenomena. Images of Si with doped nanostructures prove a conductance sensitivity corresponding to 10^{16} cm^{-3} mobile carriers, at 50 nm spatial resolution. © 2018 Optical Society of America under the terms of the OSA Open Access Publishing Agreement

1. INTRODUCTION

Scattering-type scanning near-field optical microscopy (s-SNOM) provides ~20 nm resolution at any frequency from ultraviolet to microwave [1], where the far-infrared region is in high demand in solid-state physics. Signatures of Drude-type semiconductors allow quantification of carrier concentration to low values, while signatures of non-Drude materials such as transition metal oxides and organic conductors reveal underlying rich physics of correlated electrons entangled by charge, orbital, spin, and lattice degrees of freedom [2]. Such behavior leads to exotic materials like correlated quantum matter, highly susceptible to external perturbation and hence showing intrinsic phase complexities, examples of which are unconventional superconductors, multiferroics, or Mott insulators [3]. Characteristic length scales of intrinsic phase separation reach far below an infrared wavelength and thus call for applying advanced near-field nanoscopy methods that have emerged over the past two decades. In s-SNOM, a metal AFM tip is illuminated by a focused light that concentrates at the tip apex and interacts with a sample. Scattered light is coherently detected, simultaneously with topography, such that scanning generates two optical images, one of the scattering efficiency amplitude s, the other of the phase φ of scattering [1]. A former attempt at far-infrared s-SNOM imaging suffered from demanding instrumentation, especially a liquid He-cooled detector with

inadequate dynamic range that was inadequate for determining phase contrast [4]. Pioneering microwave s-SNOMs [5,6] based on waveguide-connected tips demonstrated [5] the principle of tip-confined optical nanoscopy, the use of interferometry to record amplitude and phase images, and the value of electrostatic theory for understanding the near-field interaction mechanism. Here, we introduce a terahertz (THz) s-SNOM where a high-frequency microwave circuit connects via free space with a standard s-SNOM (Fig. 1) and achieves high S/N and thus fast imaging, with no need to use a beamsplitter for cooling, or an external detector.

2. EXPERIMENT

The THz transceiver, custom-built by Virginia Diodes Inc., features high-harmonic (54th) generation of a synthesized microwave at frequency ω, which is precisely and quickly tunable from 9 to 14 GHz, to launch a vertically polarized, diverging THz beam of ~10 µW from a 1.3 mm × 2.5 mm aperture, tunable from 0.5 to 0.75 THz. The solid-state multiplication chain consists of transistor-based amplifiers and Schottky diodes mounted in a hollow metal waveguide (depicted as red in the circuit scheme of Fig. 1). By band filtering and the use of balanced multiplier designs, a clean 54th-harmonic output is achieved. In addition, the transceiver redirects any THz radiation that propagates backward from the launching aperture via an internal
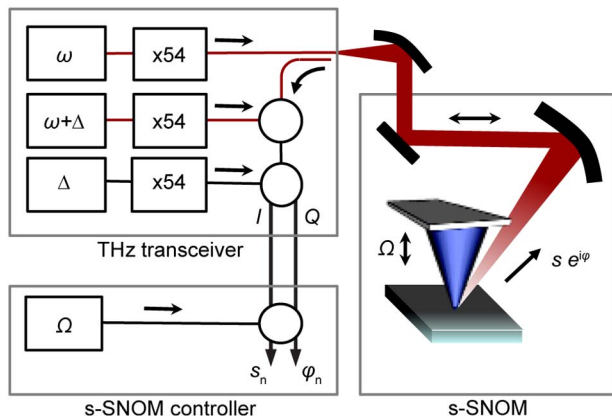
Fig. 1. Sketch of s-SNOM illuminated by a free-space THz beam, tunable between 0.5 and 0.75 THz, from a microwave–harmonic transceiver circuit that also provides heterodyne detection of back-propagating THz waves and generates output signals I and Q. These signals become demodulated in the s-SNOM controller at low-order harmonics n of the tip tapping frequency Ω, to generate simultaneous, background-free near-field amplitude and phase images together with topography.

waveguide directional coupler, and downconverts it to a 50 MHz signal using a Schottky diode mixer (see operation principle in Supplement 1) depicted as the upper circle in Fig. 1. For this heterodyne detection process, in our realization of backscattered THz light from the probing tip, the reference wave is generated by ×54 multiplication of a synthesized microwave at frequency $\omega + \Delta$ with $\Delta = 0.926$ MHz chosen such that the mixer generates the IF (intermediate frequency) signal at a fixed frequency of $54 \times 0.926 = 50$ MHz, independently of the tuning of ω (i.e., of both THz frequencies).

A single 90° off-axis paraboloidal mirror of 50 mm effective focal length couples the THz beam to and from a standard s-SNOM (NeaSNOM of Neaspec GmbH; see photograph in Supplement 1 [Fig. S1]); its alignment is facilitated by a pilot beam (not shown) from the second, opposite input port of the NeaSNOM. A commercial full-metal tip of 80 µm shaft length (Rocky Mountain 25PT200B-H), five times longer than in common infrared s-SNOMs, provides sizable (even if not optimal) antenna efficiency at the long wavelength of 500 µm corresponding to 0.6 THz. An initial alignment of the s-SNOM's internal paraboloidal mirror is uncritical as expected from the large focal volume.

Note that the IF signal faithfully replicates amplitude s and phase φ of the tip-backscattered THz radiation, and furthermore, that the present scheme is a low-frequency analog of the first heterodyne, complex-contrast and background-free s-SNOM that worked in the visible [7]. The IF signal is fed to an I-Q Schottky mixer, depicted as the middle circle in Fig. 1, together with a reference signal at $54 \times \Delta$. This unit forms two output signals, I and Q, because it contains two mixers of which one has its reference wave delayed by 90°. Both are fed into the standard electronics controller of the s-SNOM, which determines their modulation components simultaneously for several harmonics of the tip tapping frequency Ω. Recall the tip oscillates normally to the sample surface; in this work with 200 nm amplitude, it oscillates at the cantilever's resonance frequency of 70 KHz. Selecting a component with a harmonic number high enough guarantees suppression of unwanted background-scattered radiation, and thus pure near-field imaging [1]. A unique practical advantage of synthesized microwaves is their

tight control of frequency to <1 Hz, because this allows a temporarily offsetting of Δ by a few Hz, such that both I-Q mixer outputs visibly oscillate between their extreme levels and thus facilitate the final alignment of the s-SNOM's internal paraboloidal mirror in all translational degrees of freedom.

3. RESULTS

The THz s-SNOM's performance is demonstrated with an all-Si sample (SRAM, available from Bruker Nano Inc.) that exhibits multiply repeated nanostructures of various doping levels and also high topographic steps that allow their recognition in any microscope. Figure 2 displays the 0.6 THz image (cut from the larger one in Supplement 1, Fig. S2, left) of the SRAM sample. Both amplitude s_3 and phase φ_3 images exhibit topography-induced stripes next to high topography steps due to an "edge-darkening" effect [1]. Otherwise, the THz images distinguish several regions with differing amplitude and phase contrasts, indicating varied conditions of the free carrier population; namely, carrier type, density, and mobility. In passing, note dark dots in the amplitude image that correlate with topography humps; we assign them to low-refractive-index dust particles of about 50 nm height, preventing the tip from reaching the surface whereby they reduce the strength of the near-field interaction but not its phase. Four regions (A–D) are depicted in Fig. 2 by dashed boxes, which show homogeneous THz contrasts and are assigned by the supplier of
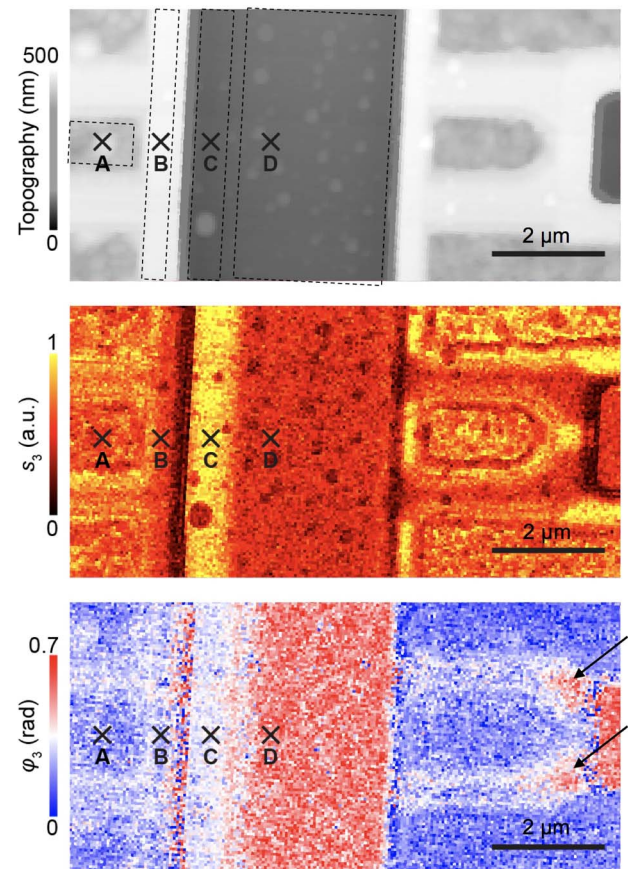

Fig. 2. Single-frequency 0.6 THz s-SNOM of Si exhibiting topographical as well as doping nanostructures, namely, the simultaneously recorded topography (top), THz amplitude s_3 (mid), and THz phase φ_3 nano-images (bottom); acquisition time, 10 min.
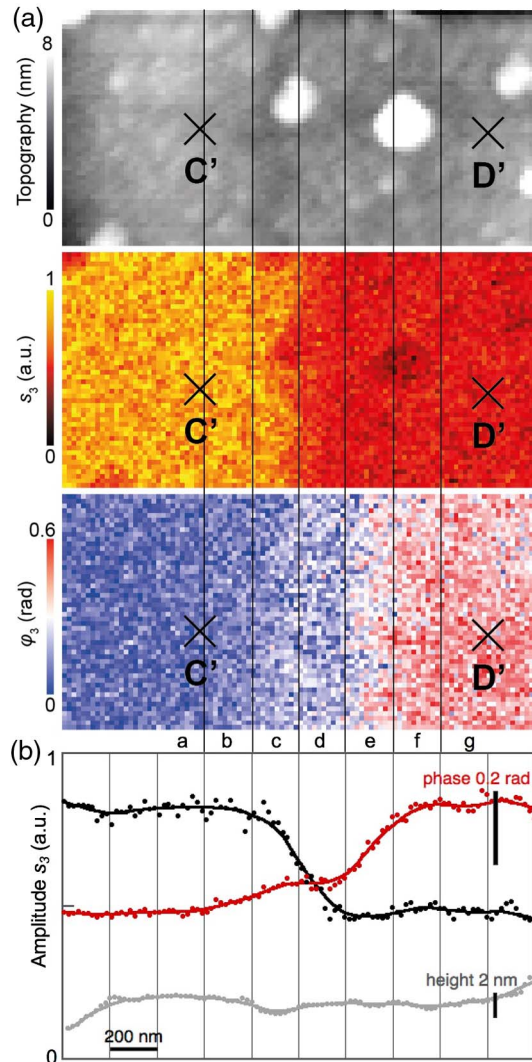
Fig. 3. Single-frequency 0.6 THz s-SNOM image (1 μm × 2 μm) of Si as in Fig. 2 extending over the edge of the ion-implanted region C'. (a) Simultaneously recorded topography (top), THz amplitude s_3 (mid), and THz phase φ_3 (bottom); acquisition time, 2.5 min; (b) Line profiles (dots) along the full 2 μm width of the image (a), height (grey), amplitude (black), and phase (red) obtained by averaging the lower 400 nm each of the respective images; curves are obtained by smoothing.

the Si test structure with the following characteristics. D is the homogeneously p-doped substrate with nominal hole density of $2 \cdot 10^{16}$ cm^{-3}. The others are ion implanted: A, p-type with hole density $4 \cdot 10^{19}$ cm^{-3}; and B and C, n-type with electron densities of $2 \cdot 10^{20}$ cm^{-3} and $2 \cdot 10^{17}$ cm^{-3}, respectively.

At the tapping amplitude of 200 nm used in Figs. 2 and 3, and Supplement 1, Fig. S2, left, the scattering signals are nearly background-free already in the second tapping harmonic, and certainly background-free in the third harmonic images presented in this work. This is proven by approach curves in the Supplement 1, Fig. S3, where the THz amplitude s_3 decays to 20% at a tip-sample distance z of about 50 nm. This behavior is compatible with the specified tip radius of the order of 50 nm, and thus, with a 50 nm lateral resolution as well as a 50 nm effective probing depth into the Si sample [1].

The arrows in the phase image of Fig. 2 point to two ∼500 nm wide regions of distinct contrast, which are not mentioned in the sample's description; also, they are not visible in its mid-infrared s-SNOM nano-image (Supplement 1, Fig. S2b). While following their origin would be beyond the scope of the present paper, they directly illustrate our method's sensitivity to low carrier density.

Next, we demonstrate the capability of 0.6 THz s-SNOM to map low carrier-density gradients, by recording a higher-resolved image of the transition region between areas C and D. The images in Fig. 3 reveal an interesting substructure across the doping edge, as each of the three observables in s-SNOM, topography, THz amplitude, and THz phase seemingly have the edge at different positions, offset up to hundreds of nm. As seen in Fig. 3(b) in detail, the amplitude decreases evenly over a ∼300 nm distance covering sections b and c; the topography features a 1 nm deep depression within section b only; the phase increases monotonically over ∼500 nm distance covering sections a to e, but stays constant within section c. Obviously, the transition between n-type and p-type regions studied here extends over a ∼500 nm distance.

4. THEORY

To understand these contrasts, we recall that the dielectric response due to charge carriers of density n_c moving freely in a neutral medium (plasma) is governed by the dynamical conductivity $\sigma(\omega)$, which in Drude approximation is constant from DC up to the plasma frequency ω_p. The plasma frequency scales with the carrier density n_c and mass m_c as $\omega_p \approx \sqrt{n_c/m_c}$, and lies in the visible for metals. Near-field interaction with a Drude-type semiconductor leads to a resonant response characterized by a phase peak and an amplitude step near ω_p, as was first predicted using the point dipole model of near-field interaction and verified experimentally at high $n_c \approx 10^{19}$ cm^{-3} in the mid-infrared [8]. The first far-infrared nano-imaging of carrier distributions at 2.5 THz [4] demonstrated sensitivity from the 10^{18} to below 10^{17} cm^{-3} range, which is centrally important for semiconductor science and technology (that demonstration was a *tour de force* because of the required, low-dynamic-range superconducting detector [4]). To focus on our observed contrasts in Fig. 3, we calculate the complex near-field response at 0.6 THz using the finite dipole model of tip-sample near-field interaction (effective tip length 600 nm, tip radius 50 nm, illumination angle 60°) [1,9]. The extended Drude dielectric data of Si were calculated from literature values for the mass and mobility of electrons and holes, respectively [10,11,12]. The theory result in Fig. 4 demonstrates a clear difference between electrons and holes, especially that a Drude resonance at 0.6 THz can arise from either an electron density of $3 \cdot 10^{16}$ cm^{-3} or a hole density of $8 \cdot 10^{16}$ cm^{-3}. Such densities are of the same order of magnitude as those specified by the sample supplier for areas C and D depicted in Fig. 2. In passing, we point out that our s-SNOM imaging of the same sample in the mid-infrared (see Supplement 1, Fig. S2) shows no contrast in areas C and D; indeed, at that 45-fold higher frequency (27 THz), a Drude resonance would necessitate a 2000-fold higher carrier density.

5. DISCUSSION

The curves in Fig. 4 predict that for Si, even a single-frequency measurement of s-SNOM amplitude and phase at 0.6 THz can
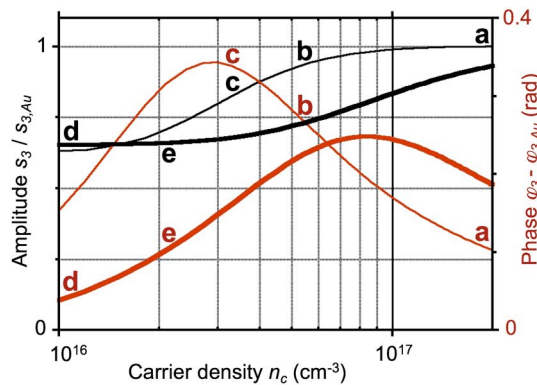
Fig. 4. Predicted 0.6 THz s-SNOM scattering amplitude s_3 (black) and scattering phase φ_3 (red) of Si, relative to Au, versus carrier density for electrons (thin curves) and holes (thick curves). Letters tentatively placed next to these curves correspond to the sections a–e of the n-p transition region investigated in Fig. 3.

both identify the carrier type and quantify the carrier density in the 10^{16} to $>10^{17}$ cm^{-3} range. To do so, the mass and mobility of electrons and holes must be known and the measurement must be calibrated with a known reference material such as Au. This calibration was not attempted in the present study, however, considering that the unknown depth profile of ion implantation in area C should cause problems of interpretation. Clearly, a similarly qualitative and quantitative material characterization is possible with our method, not only for doped semiconductors but for any conducting or even dielectric system whose dielectric function exhibits contrast in the THz region.

The predictions of Fig. 4 can qualitatively explain several features of the experimental near-field profiles of Fig. 3(b). Consider first the region D', which represents p-type Si substrate of nominal density $n_h = 2 \cdot 10^{16}$ cm^{-3}, certainly a standard substrate homogeneous throughout the depth of the probing near-field into the sample. Approaching the edge of the doped area C', starting from around D' along sections e and d, reveals that the phase decreases but the amplitude stays constant, just as predicted by the thick curves in Fig. 4, for the case that n_h decreases from about $2 \cdot 10^{16}$ cm^{-3} to a lower value because of recombination with electrons. A second example is the approach to the edge from around C' along sections a, b, and c, where we observe a decreasing amplitude and an increasing phase, also just as Fig. 4 (thin curves) would predict for an electron density decrease from $n_e \approx 2 \cdot 10^{17}$ cm^{-3} to $\approx 3 \cdot 10^{16}$ cm^{-3}. Other observed features, such as a mismatch of predicted phases in sections c and d close to the edge, need further consideration that goes beyond the scope of this paper. In fact, the significant depression of the surface in section b is an indication that the doping/annealing process may have produced a more complex nanostructure in the n-p transition than simple in-plane density gradients (one process step for area C' was implanting 900 kV P^+ ions that, according to literature, deposit acceptors primarily in 1 ± 0.5 μm depth below the surface).

6. OUTLOOK

There are two promising extensions of the presented nano-imaging, which would allow further insight. One is the established tomography method of s-SNOM, which can detect sub-surface layers and quantify depth profiles by systematically varying the tapping conditions or analyzing different demodulation orders [12–15]. The other is to repeat nano-imaging at precisely varied (>8 digits of precision) transceiver frequencies anywhere between 0.5 and 0.75 THz with the present device (0.75 to 1.1 THz with a new model being developed). Tuning can currently be achieved within 3 ms and should enable fast spectroscopic s-SNOM acquiring half-octave-wide THz point spectra in a matter of seconds. For comparison, time-domain THz nano-spectroscopy covering a decade of frequencies centered around 0.7 THz has matured from early demonstrations [16,17] into a commercial product (neaspec.com) that has recently enabled taking amplitude-and-phase point spectra of the present sample in a few min/pixel acquisition time [18,19].

7. CONCLUSION

We conclude that our all-electronic THz nano-imaging is capable of quantifying conductivity of lowly doped semiconductors not only on the 50 nm scale in a matter of few min acquisition time for a 10,000 pixel image, but also at sub-order-of-magnitude precision in carrier density, including identification of carrier type, without a calibration procedure, as required with microwave-impedance-measuring AFMs [6,20]. Moreover, all-electronic THz s-SNOM is ready for correlative microscopy using infrared or Raman channels to be operated from the second port of the NeaSNOM nanoscope. A practical advantage of our all-electronic THz nanoscope is that THz generation and coherent detection are both contained and permanently aligned inside a compact device. No cryogenic detectors are needed, as is the case with lasers or synchrotrons, and, indeed, no external detector must be operated, as with time-domain THz systems.

All-electronic THz nanoscopy opens up fast and simple nanoscale probing to a wealth of actively studied physics phenomena and materials exhibiting low, exotic, and/or non-Drude conduction mechanisms, such as in high-Tc superconductivity, ballistic transport, charge density wave, or electronic phase separation, in conventional as well as in quantum materials like topological insulators and polaritonic two-dimensional materials, or in molecular electronics.

See Supplement 1 for supporting content.

REFERENCES

1. F. Keilmann and R. Hillenbrand, "Near-field nanoscopy by elastic light scattering from a tip," in *Nano-Optics and Near-Field Optical Microscopy*, A. V. Zayats and D. Richards, eds. (Artech House, 2009).
2. S. V. Dordevic and D. N. Basov, "Electrodynamics of correlated electron matter," Ann. Phys. **15**, 545–570 (2006).
3. M. Liu, A. J. Sternbach, and D. Basov, "Nanoscale electrodynamics of strongly correlated quantum materials," Rep. Prog. Phys. **80**, 014501 (2016).

4. A. J. Huber, F. Keilmann, J. Wittborn, J. Aizpurua, and R. Hillenbrand, "Terahertz near-field nanoscopy of mobile carriers in single semiconductor nanodevices," Nano Lett. **8**, 3766–3770 (2008).

5. F. Keilmann, D. W. V. D. Weide, T. Eickelkamp, R. Merz, and D. Stöckle, "Extreme sub-wavelength resolution with a scanning radio-frequency transmission microscope," Opt. Commun. **129**, 15–18 (1996).

6. A. Imtiaz, S. M. Anlage, J. D. Barry, and J. Melngailis, "Nanometer-scale material contrast imaging with a near-field microwave microscope," Appl. Phys. Lett. **90**, 143106 (2007).

7. R. Hillenbrand and F. Keilmann, "Complex optical constants on a sub-wavelength scale," Phys. Rev. Lett. **85**, 3029–3032 (2000).

8. B. Knoll and F. Keilmann, "Infrared conductivity mapping for nanoelectronics," Appl. Phys. Lett. **77**, 3980–3982 (2000).

9. A. Cvitkovic, N. Ocelic, and R. Hillenbrand, "Analytical model for quantitative prediction of material contrasts inscattering-type near-field optical microscopy," Opt. Express **15**, 8550–8565 (2007).

10. G. Masetti, M. Severi, and S. Solmi, "Modeling of carrier mobility against carrier concentration in arsenic-, phosphorus-, and boron-doped silicon," IEEE Trans. Electron. Devices **30**, 764–769 (1983).

11. D. M. Riffe, "Temperature dependence of silicon carrier effective masses with application to femtosecond reflectivity measurements," J. Opt. Soc. Am. B **19**, 1092–1100 (2002).

12. J. M. Stiegler, A. J. Huber, S. L. Diedenhofen, J. Gomez Rivas, R. E. Algra, E. Bakkers, and R. Hillenbrand, "Nanoscale free-carrier profiling of individual semiconductor nanowires by infrared near-field nanoscopy," Nano Lett. **10**, 1387–1392 (2010).

13. J. Sun, J. C. Schotland, R. Hillenbrand, and P. S. Carney, "Nanoscale optical tomography using volume-scanning near-field microscopy," Appl. Phys. Lett. **95**, 121108 (2009).

14. M. Eisele, T. L. Cocker, M. A. Huber, M. Plankl, L. Viti, D. Ercolani, L. Sorba, M. S. Vitiello, and R. Huber, "Ultrafast multi-terahertz nanospectroscopy with sub-cycle temporal resolution," Nat. Photonics **8**, 841–845 (2014).

15. K. Moon, H. Park, J. Kim, Y. Do, S. Lee, G. Lee, H. Kang, and H. Han, "Subsurface nanoimaging by broadband terahertz pulse near-field microscopy," Nano Lett. **15**, 549–552 (2014).

16. F. Buersgens, H.-T. Chen, and R. Kersting, "Terahertz microscopy of charge carriers in semiconductors," Appl. Phys. Lett. **88**, 112115 (2006).

17. H.-G. von Ribbeck, M. Brehm, D. W. van der Weide, S. Winnerl, O. Drachenko, M. Helm, and F. Keilmann, "Spectroscopic THz near-field microscopy," Opt. Express **16**, 3430–3438 (2008).

18. F. Huth and Y. Abate, (personal communication, 2017).

19. M. C. Giordano, S. Mastel, C. Liewald, L. L. Columbo, M. Brambilla, L. Viti, A. Politano, K. Zhang, L. Li, A. G. Davies, E. H. Linfield, R. Hillenbrand, F. Keilmann, G. Scamarcio, and M. S. Vitiello are preparing a manuscript to be called "Phase-resolved terahertz self-detection near-field microscopy."

20. A. Imtiaz, T. M. Wallis, S.-H. Lim, H. Tanbakuchi, H.-P. Huber, A. Hornung, P. Hinterdorfer, J. Smoliner, F. Kienberger, and P. Kabos, "Frequency-selective contrast on variably doped p-type silicon with a scanning microwave microscope," J. Appl. Phys. **111**, 93727 (2012).